RESEARCH ARTICLE

FUNDAMENTAL PHYSICS

Two-photon frequency comb spectroscopy of atomic hydrogen

Alexey Grinin[1]*, Arthur Matveev[1], Dylan C. Yost[1]†, Lothar Maisenbacher[1], Vitaly Wirthl[1], Randolf Pohl[1]‡, Theodor W. Hänsch[1,2], Thomas Udem[1,2]

We have performed two-photon ultraviolet direct frequency comb spectroscopy on the 1S-3S transition in atomic hydrogen to illuminate the so-called proton radius puzzle and to demonstrate the potential of this method. The proton radius puzzle is a significant discrepancy between data obtained with muonic hydrogen and regular atomic hydrogen that could not be explained within the framework of quantum electrodynamics. By combining our result [$f_{1S\text{-}3S}$ = 2,922,743,278,665.79(72) kilohertz] with a previous measurement of the 1S-2S transition frequency, we obtained new values for the Rydberg constant [R_∞ = 10,973,731.568226(38) per meter] and the proton charge radius [r_p = 0.8482(38) femtometers]. This result favors the muonic value over the world-average data as presented by the most recent published CODATA 2014 adjustment.

Quantum electrodynamics (QED) is widely considered to be the most developed fundamental theory. It served as the blueprint for other quantum field theories and is capable of predicting the energy levels of atomic hydrogen and the electron *g*-factor with an accuracy of 12 digits. It is of fundamental interest to experimentally verify all of these digits or to discover tiny discrepancies that may lead to new physics.

The QED theory for the energy levels of atomic hydrogen can be cast in the form

$$E_{n,\ell,j} = chR_\infty\left(-\frac{1}{n^2}+f_{n,\ell,j}\left(\alpha,\frac{m_e}{m_p},\ldots\right)+\delta_{\ell,0}\frac{C_{NS}}{n^3}r_p^2\right) \quad (1)$$

with n, ℓ and j being the principle quantum number and the orbital and total angular momentum, respectively. The well-known leading term is obtained from both the Bohr and Schrödinger theories. The function $f_{n,\ell,j}$ is a lengthy but mostly analytic expression (*1*) that depends, among other things, on the fine structure constant α and the electron-to-proton mass ratio m_e/m_p. These constants can be obtained with sufficient accuracy from other experiments where they do not merely represent a correction to a much larger term (*2*, *3*). The last term is a small but important correction to S-states owing to the finite root-mean-square (RMS) charge radius of the proton r_p. To convert to SI units (International System of Units) used in the experiment, the full theory expression needs to be multiplied by the Rydberg energy, chR_∞.

By accurately measuring transition frequencies, i.e., differences of energy levels, values for R_∞ and r_p can be obtained simply by treating them as parameters and adjusting their values to match the experimental observations. Two measured transition frequencies are required to determine the values of the two parameters, and the second most accurate measurement sets the limit on the uncertainty of R_∞ and r_p. If QED, its usage, and the experiments are all correct, a self-consistent set of the parameter values is expected when using all available measured transition frequencies (*4*). However, a serious discrepancy to existing hydrogen data was found when high-resolution laser spectroscopy on muonic hydrogen first became possible (*5*). This exotic atom is analogous to regular atomic hydrogen, but with the electron replaced by its heavier, short-lived sibling, the muon. Its energy levels should obey the same QED formalism but with an approximately four orders of magnitude larger coefficient C_{NS} and a corresponding increased sensitivity to r_p. A discrepancy of four standard deviations (4σ) was found when comparing r_p obtained in this way with the values obtained from regular atomic hydrogen. This fact has motivated additional high-precision spectroscopy of atomic hydrogen (*6*–*8*). These more recent measurements are discussed below.

The proton charge radius can also be obtained from electron-proton scattering with results that either support the muonic value (*9*, *10*) or elevate the discrepancy associated with the proton radius puzzle (*1*). Because there is no QED expression like Eq. 1 for the proton charge distribution, electron scattering data cannot directly contribute to testing QED. Using consistent scattering data could improve the values of R_∞ and r_p. However, here we are less interested in these values and more interested in checking for consistency of their QED-dependent determinations.

We report a measurement that considerably reduces the uncertainty of the 1S-3S transition frequency, which is the second most precisely known transition frequency in atomic hydrogen. It is surpassed only by the 1S-2S transition (*11*), which has a natural line width that is several orders of magnitude smaller than any other relevant transition in atomic hydrogen. We have substantially reduced the systematic uncertainties and required corrections by using a cold atomic beam and by utilizing the advantages of the direct frequency comb technique. An almost shot noise limited statistical uncertainty of only 110 Hz has been obtained with small systematic effects whose compensation does not critically rely on model

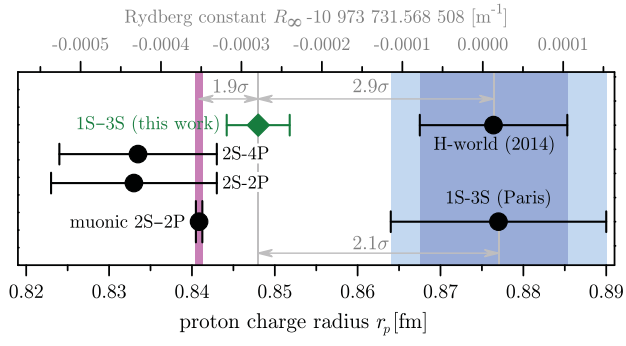

Fig. 1. Proton charge radius measurements. The proton charge radius measurements (bottom axis), as obtained from various experiments, partially disagree, preventing a verification of quantum electrodynamics at the level of experimental uncertainties. Combining the 1S-2S and the 1S-3S (this work) transition frequencies in atomic hydrogen gives a significantly smaller value than the previous world data [H-world (2014)] obtained by using all hydrogen measurements (15 lines) available for the most recent published CODATA 2014 adjustment [Adj #8, table XXIX in (*1*)]. In contrast, a recent continuous wave measurement of the 1S-3S transition frequency [1S-3S (Paris)] (*7*) confirms the CODATA value. Our result is in reasonable agreement with a value derived from the previous 2S-4P measurement (*6*), with a radio frequency measurement of the 2S-2P transition (*8*), and with the value obtained from muonic hydrogen (*32*). Because of the strong correlation (98.91%) between R_∞ and r_p, the data can also be displayed in terms of the Rydberg constant (same graph, upper axis).

[1]Laser Spectroscopy Division Max-Planck-Institut für Quantenoptik, Garching, Germany. [2]Department of Physics, Ludwig-Maximilians-Universität, München, Germany.
†Present address: Department of Physics, Colorado State University, Fort Collins, CO, USA.
‡Present address: Institut für Physik, Johannes Gutenberg-Universität Mainz, Mainz, Germany.
*Corresponding author. Email: alexey.grinin@mpq.mpg.de

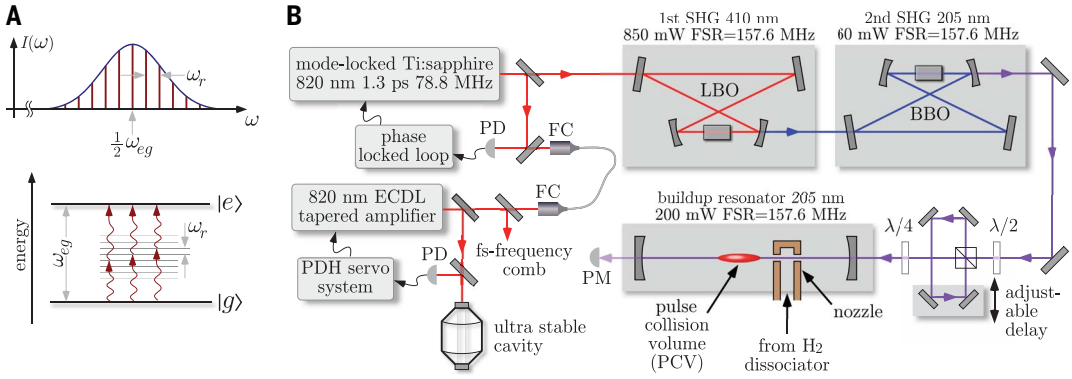

Fig. 2. Principle and experimental setup for two-photon direct frequency comb spectroscopy. (**A**) Spectral envelope of the frequency comb with repetition rate ω_r (not to scale) tuned to excite a two-photon transition between $|g\rangle$ and $|e\rangle$ at the frequency ω_{eg}. On resonance, pairwise addition of properly phased modes provides an efficient excitation of the atoms. (**B**) A mode-locked titanium sapphire laser (78.8 MHz, 1.3 ps, 2.8 W) is referenced to a transfer laser that is itself locked to an ultrastable cavity and referenced to a femtosecond-frequency comb. This frequency comb is then frequency quadrupled in two successive intracavity doubling stages to generate a deep ultraviolet frequency comb at 205 nm. The optical cavities used for frequency doubling are built with half the length of the fundamental laser cavity, which effectively doubles the repetition rate of the quadrupled frequency comb to 157.6 MHz. The pulse train is then sent to a beam splitter and delay line used to generate counterpropagating pulses within a final enhancement cavity where the hydrogen spectroscopy takes place. PM, power meter; FC, fiber coupler; FSR, free spectral range; PDH, Pound-Drever-Hall stabilization (*33*); ECDL, extended cavity diode laser; SHG, second-harmonic generation; LBO/BBO, lithium triborate and β–barium borate crystals; PD, photodetector.

assumptions. In addition, we used the simple Lorentzian line shape model and found the line center within 10^{-3} of the line width, which is a rather moderate value.

With this experiment, we also demonstrate high-resolution laser spectroscopy with a harmonic frequency comb in the ultraviolet region. The associated short pulses of the frequency comb make the harmonic generation process in crystals and gas targets more efficient, while avoiding the photorefractive effect (*12*). In the future, this method may allow precision spectroscopy at even shorter unexplored wavelength regions using high harmonic generation—hopefully enabling high-resolution laser spectroscopy of hydrogen-like ions (*13*).

Combining the results for the 1S-3S and the 1S-2S transitions, we extracted values for the Rydberg constant R_∞ and the proton charge radius r_p. These new values are two times more accurate than the ones obtained from all previous hydrogen data combined. By using only two measurements to determine two constants (treated as parameters), nothing can be said about the validity of QED. It does not matter whether we use the Rydberg constant or the proton charge radius for a consistency check, because the values of these parameters are strongly correlated through Eq. 1. This work favors the data from muonic hydrogen and a recently improved measurement of the 2S-2P Lamb shift in regular hydrogen (*8*). Further, our value is in good agreement with a recent measurement of the 2S-4P interval (*6*) but disagrees by 2.9σ with the hydrogen world data obtained by CODATA 2014 (*1*). Figure 1 summarizes the situation.

Two-photon direct frequency comb spectroscopy

An optical frequency comb is a regularly spaced array of laser frequencies $\omega_n = n\omega_r + \omega_0$ that is readily generated with a mode-locked laser (*14*). The pulse repetition rate, ω_r, is around $2\pi \times 315.2$ MHz, and the offset frequency, ω_0, is always smaller than ω_r. The integer n labels the ≈3000 laser lines (or modes) around $n \approx 1.16 \times 10^6$. During the measurements, the frequency of one of the laser modes and the exact repetition rate were constantly recorded with the help of a second, self-referenced frequency comb ("fs–frequency comb" in Fig. 2) (*15*) and a radio frequency counter, respectively. Both were referenced to a global positioning system (GPS)–disciplined hydrogen maser.

Our spectrometer is sketched in Fig. 2 and described in more detail in (*16*–*18*). Briefly, the carrier frequency of a mode-locked titanium: sapphire laser (78.8 MHz, 1.3 ps, 2.8 W) was doubled in an enhancement resonator with half the optical length of the laser resonator. This arrangement also doubled the repetition rate. After a second doubling stage that left the repetition rate constant, we obtained up to 50 mW of 205-nm radiation with a full width half maximum (FWHM) pulse duration of 2.0 ps (*18*). A delay line generated σ^+/σ^- circular-polarized double pulses that met twice per round trip at the center of the enhancement cavity housed in a vacuum chamber. This doubled the repetition rate once more to 315.2 MHz. Our general effort to produce a high repetition rate, both through the doubling stages and with the use of the delay line, led to a relatively short two-mirror enhancement cavity that supported two counterpropagating pulses. Our choice of polarization avoided loss of power in the delay line and reduced the excitation of the 1S-3D transitions relative to the 1S-3S transitions. The time-averaged circulating power in this cavity was ~60 mW per propagation direction with a beam radius at the focus of w_0 = 80 μm. Hydrogen atoms were produced by dissociation of hydrogen molecules in a radio frequency discharge tube, which were then guided through a Teflon tube to a cryogenic copper nozzle. In this nozzle, they thermalized and escaped into the vacuum through two adjacent holes. Some of the atoms made it into the cigar-shaped laser pulse collision volume (PCV) and were excited to the 3S state, from which they decayed within 0.16 μs to the 2P state, releasing a detectable 656-nm Balmer–α photon (Fig. 3).

To drive a two-photon transition with a frequency comb, the photon energies associated with the laser modes add up pairwise to produce the transition energy $h\omega_{eg}$ (*19*). By tuning ω_r such that a particular comb mode ω_n corresponds to half the transition frequency, all mode pairs m that satisfy the relation $\omega_{eg} = \omega_{n-m} + \omega_{n+m}$ contribute to the excitation rate. This is sketched on the left-hand side of Fig. 2. The two-photon resonance condition is also satisfied when the transition occurs exactly between two comb modes. Therefore, the spectroscopic signal repeats with the repetition rate when measured at the atomic frequency. All transitions accessible with the spectral bandwidth of the comb are observed to be convoluted within the range of ω_r.

An important feature of two-photon spectroscopy is that the first-order Doppler effect is suppressed when the atom absorbs a pair of counterpropagating photons. This can take place only within the PCV, where the excitation paths (shown in Fig. 2) add constructively. Outside the PCV, only Doppler-broadened absorption of two photons from either side takes place. The transition matrix elements for all four combinations of absorbed photon directions are the same but must be weighted by the number of atoms in the proper velocity class for Doppler-broadened absorption and by appropriately accounting for the polarization and the hyperfine structure (*20*).

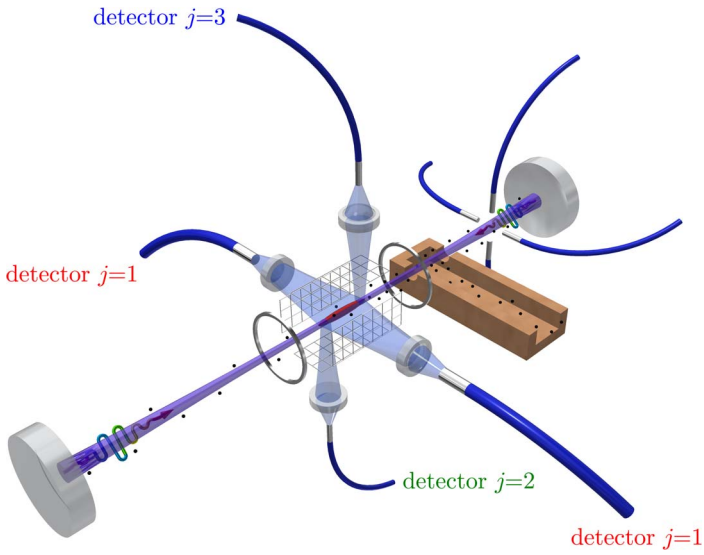

Fig. 3. Spectroscopy setup. The pulse collision volume (PCV; shown in red here and in Fig. 2) resembles an ellipsoid with semi-axes w_0 = 80 μm and $cT_{1/2}$ = 600 μm. It is surrounded by a Faraday cage made of a highly transmissive mesh and two end-cap electrodes. In the actual apparatus, the end caps cover a much larger surface around the PCV but are drawn as thin rings here for clarity. Using the quadratic DC-Stark shift, we can put tight limits on stray electric fields by applying voltages to the cage in all three directions and determining the minima of the resulting line shifts. Four lenses image the fluorescence from the whole PCV and its ends to multimode fibers (1 mm and 600 μm diameter) that guide the light through interference filters onto three independent single-photon counting modules: one main detector (j = 1) and two auxiliary detectors (j = 2, 3). With this arrangement, we can interpolate the chirp-induced residual first-order Doppler shift (CIFODS). At the other side of the nozzle, the Doppler-broadened signal is collected with four bare fibers of 1 mm core diameter that are in close proximity to the laser and atomic beam. As the Doppler-broadening is well in excess of the mode spacing, this signal is independent of the laser frequency and used for normalization. In this way, we remove substantial fluctuations of the laser power and the atom number flux. Because the Doppler-free and the Doppler-broadened signals scale in the same way with laser power, the normalized line amplitudes can be used as a measure of the atomic flux.

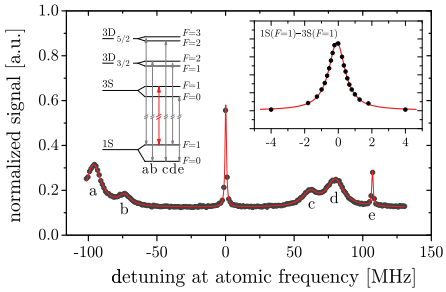

Fig. 4. Line components. Multiple 1S-3S/D two-photon transitions folded with the frequency comb so that the separation of the line components appears modulo $\omega_r = 2\pi \times 315.2$ MHz. By operating a well-chosen ω_r and with circular polarization, we obtain a well-isolated 1S(F=1)–3S(F=1) component. Other components that are allowed by the selection rules are: a, 1S(F=1)–3D$_{5/2}$; b, 1S(F=0)–3D$_{3/2}$(F=2); c, 1S(F=0)–3D$_{5/2}$(F=2); d, 1S(F=1)–3D$_{3/2}$; e, 1S(F=0)–3S(F=0). The hyperfine splitting of the 3D states is smaller than the natural line width and thus unresolved. The baseline offset is from the Doppler-broadened absorption of two copropagating photons. The inset shows an average of five line scans (3 min) within ±4 MHz of the main component, normalized to the Doppler-broadened signal, together with a Lorentzian fit. The sampling of the frequency axis was chosen to yield an approximately equidistant spacing on the signal axis to maximize the sensitivity to the center frequency per unit of measurement time. The line pulling by other 1S-3D lines and others (not visible) is negligible and discussed in detail in the SM. The detuning in this graph is measured at the atomic frequency, i.e., around the frequency given in Eq. 4. a.u., arbitrary units.

Two-photon direct comb spectroscopy is not fully free of the first-order Doppler effect. In the frequency domain, the contributing mode pairs do not have exactly the same frequencies and, thus, do not have exactly opposite Doppler shifts. However, for each pair m there is a pair $-m$ such that the Doppler shift is balanced provided that the spectral envelopes of the counterpropagating pulses are identical. This condition is best fulfilled within an enhancement resonator. As a result, the Doppler effect only broadens the line but does not shift it. In the time domain, this broadening is understood as time-of-flight broadening. Atoms with the most probable thermal velocity of v_0 = 340 m/s contribute the most to the signal at 7 K [see the supplementary materials (SM)]. When traveling along the laser beam axis, the time-of-flight broadening amounts to $\Delta\omega = 8\ln(2)v_0/cT_{1/2} = 2\pi \times 500$ kHz. By using a pulse duration (FWHM) of $T_{1/2}$ = 2 ps, we adapt the lengths of the PCV $cT_{1/2}$ such that we reach the natural line width of 1.0 MHz despite the 148 GHz wide spectral envelope of the comb (see SM).

The frequency comb in this application is, in many ways, equivalent to a continuous laser—the laser-limited line width is given by the width of a single comb mode rather than by the spectral envelope of the comb, while the line strength is given by the total power of all modes (*21*). Similarly, the AC-Stark shift derives from the time-averaged laser intensity rather than from the much larger peak intensity (*22*). Two-photon direct comb spectroscopy offers several advantages, such as access to shorter wavelengths through more efficient nonlinear processes. The small PCV allows for better control over several systematic effects and makes light collection simple and efficient. In addition, the small PCV allows for good shielding from stray electric and magnetic fields that would otherwise be challenging to compensate over a larger excitation volume. Moreover, the distance of the PCV from the nozzle can be varied to control the atomic density in a defined way to determine the pressure shift, keeping the inhomogeneities of the fields and pressure small. Although Doppler-free excitation takes place only within the PCV, Doppler-broadened fluorescence can be collected separately outside of the PCV. This signal is almost independent of the laser frequency and can be used to normalize fluctuations of laser power and atomic flux. By utilizing this feature, we could reach an almost shot-noise limited statistics (see SM). Figure 3 shows a close look at the PCV (red region) together with the shields and the detection optics that have been left out of Fig. 2. Figure 4 shows a typical line scan obtained with this spectrometer.

Data analysis and systematics

Our dataset consists of i = 1...4450 line scans like the one shown in the inset of Fig. 4, each of ≈36 sec duration. A large fraction of the data (2020 line scans) have been recorded with a nozzle temperature of 7 K. As a first step of the evaluation, we fit Lorentzians to the normalized signal to find the line widths, amplitudes, constant offsets, and the center frequencies $f_{j,i}$ for the three detectors (j = 1...3). The statistical uncertainties of the center frequencies $\sigma_{j,i}(f)$ are dominated by shot noise.

A small amount of excess noise is well explained by limitations of the normalization procedure and is taken into account as described in the SM. The lines recorded with the downstream detector ($j = 2$) at the lowest nozzle temperatures show the smallest time-of-flight broadening and reach the natural line width (see SM for details).

A systematic frequency shift that is intrinsic to the two-photon pulsed excitation of an atomic beam arises owing to a possible chirp of the laser frequency. To illustrate this effect, we consider Gaussian pulses counterpropagating along the $\pm z$ axis with a linear frequency chirp

$$E_{\pm}(t) = E_0 e^{-(1+ib)(t\pm z/c)^2/\tau^2 - i\omega_c t} \quad (2)$$

Here, ω_c is the carrier frequency, b is the chirp parameter, and the FWHM pulse duration is given by $T_{1/2} = \tau\sqrt{2\ln(2)}$. The Doppler-free complex Rabi frequency of this transition is proportional to $E_+(t)E_-(t) = E_0^2 e^{-2(1+ib)(t^2+z^2/c^2)/\tau^2 - i2\omega_c t}$, where the fast oscillating carrier drops out within the usual rotating wave approximation. Any remaining time-dependent phase can translate into a frequency shift. This does not apply to the first phase term in the exponent, because in a repetitive pulse train, it merely leads to a periodic phase modulation without affecting the comb structure. The second phase term, however, acquires a time dependence with the changing position of the atom and leads to an instantaneous position-dependent frequency shift of $4bzv_z/c^2\tau^2$. With its dependence on velocity v_z, this frequency shift appears as a residual chirp-induced first-order Doppler shift (CIFODS) (*16*). In practice, the CIFODS is largely reduced because atoms are probed at positions of positive and negative z [in an isotropic gas sample also with both signs of v_z (*23*, *24*)]. However, as illustrated in Fig. 5, the divergence of the atomic beam leads to an imbalance of density and hence to an imbalance of the signals received from either ends of the PCV. Assuming the distance d of the PCV to the emerging point of the atomic beam is large compared to the dimensions of the PCV, the resulting CIFODS is estimated to be $\Delta\omega \approx -bv_0/d$. From the experimental data, we obtain a mean of $\langle b\rangle = -0.119$ with a substantially larger variation between the line scans. Data has been taken with $d = 19.1(1)$ mm and $d = 27.1(1)$ mm, so that the mean CIFODS is estimated to 0.34 kHz with $v_0 = 340$ m/s. A more detailed discussion is given in the SM and in (*16*).

Although the pulses from the laser had a negative chirp, the frequency-doubling stages introduced a positive chirp, mainly through self-phase modulation (*25*). Experimentally, we can vary the latter contribution by changing the crystal position along the focused laser beam. Unfortunately, standard methods such as frequency-resolved optical gating (FROG) cannot provide reliable values for small chirp parameters of picosecond pulses. In addition, the above arguments that lead to the CIFODS are based on a largely simplified model. However, under quite general assumptions, the CIFODS is an antisymmetric function of the position z relative to the center of the PCV. We use the position dependence of the CIFODS to measure and compensate for it. To this end, we collected light from different parts of the PCV (Fig. 3). The main detector $j = 1$ showed a small sensitivity to CIFODS, because it averaged the signal over the entire PCV. In contrast, the auxiliary detectors ($j = 2, 3$) that pointed at the ends of the PCV were maximally sensitive to CIFODS with opposite signs and hence provide a sensitive probe. CIFODS can be shown to be linear in the chirp parameter for any chirp function, as long as it is given by a single parameter (see SM). Therefore we can write $f_{j,i} = f_0 + \alpha_j b_i$, where $f_{j,i}$ is the measured frequency of the i-th scan with chirp parameter b_i by the j-th detector. This frequency is shifted from the unaffected transition frequency f_0 by an amount that is proportional to the chirp parameter b_i, which is unknown but assumed to be constant during a line scan. The CIFODS sensitivities α_j are geometry dependent and therefore insufficiently known, but fixed. In principle, the α_j can be determined through simulations, which include the geometry of the detectors and the beam divergence. The expressions for the three detectors may be combined to $f_{1,i} = f_0 + \kappa_{DS}(f_{2,i} - f_{3,i})$, where $\kappa_{DS} = \alpha_1/(\alpha_2 - \alpha_3)$, $|\alpha_1| \ll |\alpha_2|$, and $\alpha_2 \approx -\alpha_3$. The unperturbed frequency f_0 can then be obtained by making a linear fit of the measured frequencies of the main detector, $f_{1,i}$, versus the difference frequency obtained with the two auxiliary detectors, $f_{2,i} - f_{3,i}$. The determination of the chirp parameters is not required, nor do we need to know the geometry, i.e., α_j. Because our data cover both signs of b, we could interpolate to the proper transition frequency. Note that, for a similar dataset, interpolation is more accurate and reliable than extrapolation.

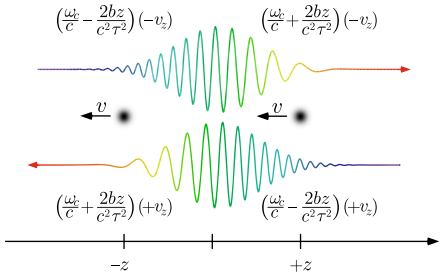

Fig. 5. Principle of the chirp-induced residual first-order Doppler shift. Two chirped counterpropagating pulses with carrier frequency ω_c (sketched spatially separated for clarity) meet within the pulse collision volume, where they drive a two-photon transition in an atom that moves parallel to the z axis with a velocity v_z. The instantaneous frequency shifts at the edges of the pulses are $\pm 2bv_z/c^2\tau^2$ at positions $\pm z$, with the chirp parameter b and with the value of the shift doubling for a two-photon transition. For the Doppler shift, the velocity has to be measured relative to the pulse propagation direction. The shifts cancel for atoms that travel exactly parallel to the z axis. In a divergent atomic beam, however, this cancellation is no longer perfect, and the CIFODS might be estimated by integrating over z with a weight given by the square of the magnitude of the Rabi frequency $\propto \exp(-4(z-d)^2/c^2\tau^2)$ with distance d between the PCV and the emerging point of the atomic beam. This results in $\Delta\omega \approx -bv/d$.

Similarly to the CIFODS interpolation, we extrapolate the AC-Stark shift by adding a term $\kappa_{AC}P_i$, where P_i are the scan-averaged cavity-transmitted laser powers (see "PM" in Fig. 2). Nonlinear effects due to saturation and ionization were negligible (<1 Hz) at the power levels used. Under average experimental conditions, the AC-Stark effect shifts the resonance by 4.6 kHz.

An additional systematic shift is the pressure shift, which is due to collisions within the atomic beam and with the residual background gas. Because the latter was estimated to be negligible (see SM), we determined the effects of the intrabeam collisions by taking advantage of the small excitation volume. By changing the PCV-to-nozzle distance, we can vary the density of atoms and molecules by about a factor of 2. The properly normalized and scaled line amplitudes (see SM for details), A_i, were used to measure the local density of atoms independently of the other fluctuations such as laser power variations. We introduce another term, $\kappa_{PS}A_i$, to extrapolate the pressure shift.

The final and somewhat larger systematic shift is due to the second-order Doppler (SOD) effect, which is given by $-(v/2c)^2$ in relative units for an atom at a velocity v. We estimate this shift to be −2.9 kHz at a nozzle temperature of $T = 7$ K by computing the average squared velocity of $\bar{v}^2 = (416\ \mathrm{m/s})^2$ for atoms with the largest contribution to the signal (see SM). Because $\bar{v}^2 \sim T$, the SOD is expected to be linear with the nozzle temperature. For a thermal atomic beam at room temperature, the SOD shift would be about −79 kHz in our geometry. The motional Stark effect can be used to compensate for this rather large shift (*26*). In our case, we instead took data at a wide range of temperatures and introduced another parameter, κ_{SOD}, that modeled the SOD shift to be linear in temperature.

In total, we adjusted

$$f_{1,i} = f_0 + \kappa_{DS}(f_{2,i} - f_{3,i}) + \kappa_{SOD}T_i + \kappa_{AC}P_i + \kappa_{PS}A_i \quad (3)$$

to the experimental data ($f_{j,i}$, T_i, P_i, and A_i) weighted by their uncertainties and correlations, by adjusting the parameters κ_{DS}, κ_{SOD}, κ_{AC}, κ_{PS}, and f_0. As discussed earlier, we believe that the CIFODS compensation is very robust. On the basis of simple perturbation theory, the AC-Stark shift is expected to be linear. The pressure shift was less well controlled, but it is the smallest of the shifts compensated by fitting Eq. 3. The effective SOD shift, even at low temperatures, required the second largest correction. In addition, linearity with temperature may be compromised by the complex velocity-dependent excitation probability and expected deviations from the Maxwellian velocity distribution. To make sure that we fully understand this effect to the required level, we took data at seven different nozzle temperatures. Because a larger SOD requires a more precise model, we decided to use only the $T \leq 30$ K data in Eq. 3. As shown in Fig. 6, this fit correctly predicts the data at higher temperatures. Therefore we are confident that the linearity assumption holds for the lower temperatures but take possible deviations into account by adding temperature-dependent model uncertainties to the uncertainties of the measured frequencies $f_{1,i}$ (see SM for details). Further corrections applied to the transition frequency, f_0, were the DC-Stark shift, the Zeeman shift, quantum interference line pulling (*27*, *28*), line pulling through other fine- and hyperfine components, and the maser calibration (the details are given in the SM).

Rydberg constant and proton charge radius

In all steps of the evaluation, the uncertainties were propagated, and correlations were taken into account. All corrections and the error budget are given in Table 1. After applying them, we obtain the unperturbed frequency of the 1S(F=1)–3S(F=1) transition

$$f_{1S\text{-}3S}(F=1) = 2{,}922{,}742{,}936{,}716.72(72)\ \text{kHz} \quad (4)$$

Subtracting the hyperfine shifts of –341,949,069.6(8) Hz (*29*) gives the hyperfine centroid

$$f_{1S\text{-}3S}(\text{centroid}) = 2{,}922{,}743{,}278{,}665.79(72)\ \text{kHz} \quad (5)$$

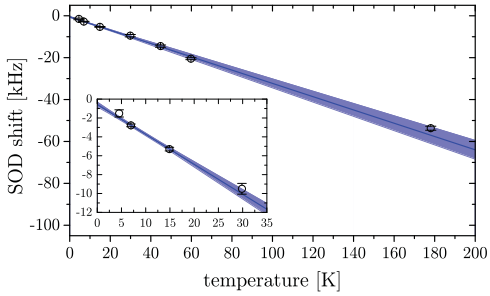

Fig. 6. Second-order Doppler. Second-order Doppler shift of the experimental data (black circles) as a function of the nozzle temperature, T, after correcting the shifts included in Eq. 3—i.e., CIFODS (κ_{DS}), AC-Stark (κ_{AC}), and pressure shift (κ_{PS}). Additional small corrections of 0.57 kHz are listed in Table 1. The error bars are obtained by assuming detection shot noise and model uncertainties as described in the text with the usual error propagation. The blue region is a linear fit together with its 1σ confidence band using the $T \leq 30$ K data only. The inset shows the low-temperature data used for evaluation in greater detail. The observed linearity justifies the use of Eq. 3. More details are given in the SM.

Table 1. Error budget of the 1S(F=1)–3S(F=1) measurement. All values are given in kilohertz. The average effect is the weighted mean of all evaluated data and quantifies the applied corrections. The multiparameter CIFODS (MP CIFODS) is an estimation of the uncertainty that may result from several independent sources of the laser chirp. This error budget is discussed in detail in the SM.

Contribution	Average effect	Correction	Uncertainty
Statistics	—	—	0.11
CIFODS	+0.79	—	0.08
SOD	−3.20	—	0.26
AC-Stark	+4.60	—	0.30
Pressure shift	+0.93	—	0.30
Residual Doppler	—	—	0.48
DC-Stark	+0.031	−0.031	0.015
Zeeman shift	−0.002	+0.002	0.002
Line pulling	−0.30	+0.30	0.050
MP CIFODS	—	—	0.10
Maser	−0.30	+0.30	0.030
Total		**+0.57**	**0.72**

This measurement is in good agreement but more than 20 times more accurate than our previous room temperature measurement (*16*) and 3.6 times more accurate than a recent 1S-3S room-temperature measurement with a continuous-wave laser (*7*). However, it deviates by 2.1 combined standard deviations from the latter. Although the combined standard deviation of our result from the muonic value is comparable, the disagreement between measurements of the same transition frequency obtained with mutually distinct leading systematic effects is of a different kind. It does not disprove QED but points to some further, yet undiscovered, systematic effects in either (or both) of these measurements.

We use our result, the measured 1S-2S transition frequency (*11*), and QED in form of Eq. 1 to improve the value for the Rydberg constant

$$R_\infty = 10{,}973{,}731.568226(38)\ \text{m}^{-1} \quad (6)$$

and obtain an independent value for the RMS proton charge radius

$$r_p = 0.8482(38)\ \text{fm} \quad (7)$$

In doing so, we have used the collection of terms provided in (*1*) as well as the values for the fine structure constant and the electron-to-proton mass ratio given there. More accurate values of these constants are available online (*30*), but that has no influence on the results presented here. An update of the theory (*31*) changes this result only within a small fraction of the error bar. The contribution to the error bar by the theory and other constants to R_∞ and r_p is 2.2×10^{-6} m^{-1} and 0.00097 fm, respectively. Our value for the Rydberg constant is more accurate than the most recent published CODATA adjustment (*1*) but differs by 3.7 combined standard deviations from it. It is, however, in agreement with the latest CODATA value that is so far available online only (*30*), without details on how this value is obtained. Our proton charge radius disagrees by 2.9 combined standard deviations from the hydrogen world data as of 2014 but is in better agreement with the most recent muonic value (*32*), a recent measurement of the Lamb shift (*8*) and the 2S-4P transition frequency (*6*) in atomic hydrogen, as well as a recent result from elastic electron-proton scattering at very low momentum transfer (*10*).

REFERENCES AND NOTES

1. P. J. Mohr, D. B. Newell, B. N. Taylor, *Rev. Mod. Phys.* **88**, 035009 (2016).
2. R. H. Parker, C. Yu, W. Zhong, B. Estey, H. Müller, *Science* **360**, 191–195 (2018).
3. F. Heiße *et al.*, *Phys. Rev. Lett.* **119**, 033001 (2017).
4. Th. Udem, *Nat. Phys.* **14**, 632 (2018).
5. R. Pohl *et al.*, *Nature* **466**, 213–216 (2010).
6. A. Beyer *et al.*, *Science* **358**, 79–85 (2017).
7. H. Fleurbaey *et al.*, *Phys. Rev. Lett.* **120**, 183001 (2018).
8. N. Bezginov *et al.*, *Science* **365**, 1007–1012 (2019).

9. I. T. Lorenz, H. W. Hammer, U. G. Meißner, *Eur. Phys. J. A* **48**, 151 (2012).
10. W. Xiong *et al.*, *Nature* **575**, 147–150 (2019).
11. A. Matveev *et al.*, *Phys. Rev. Lett.* **110**, 230801 (2013).
12. G. Hagel, F. Nez, F. Biraben, *Appl. Opt.* **41**, 7702–7706 (2002).
13. M. Herrmann *et al.*, *Phys. Rev. A* **79**, 052505 (2009).
14. M. C. Stowe *et al.*, *Adv. At. Mol. Opt. Phys.* **55**, 1–60 (2008).
15. T. Udem, R. Holzwarth, T. W. Hänsch, *Nature* **416**, 233–237 (2002).
16. D. C. Yost *et al.*, *Phys. Rev. A* **93**, 042509 (2016).
17. E. Peters, D. C. Yost, A. Matveev, T. W. Hänsch, Th. Udem, *Ann. Phys.* **525**, L29–L34 (2013).
18. E. Peters *et al.*, *Opt. Express* **17**, 9183–9190 (2009).
19. J. N. Eckstein, A. I. Ferguson, T. W. Hänsch, *Phys. Rev. Lett.* **40**, 847–850 (1978).
20. G. Grynberg, F. Biraben, E. Giacobino, B. Cagnac, *J. Phys.* **38**, 629–640 (1977).
21. Ye. V. Baklanov, V. P. Chebotayev, *Appl. Phys.* **12**, 97–99 (1977).
22. P. Fendel, S. D. Bergeson, T. Udem, T. W. Hänsch, *Opt. Lett.* **32**, 701–703 (2007).
23. S. Reinhardt, E. Peters, T. W. Hänsch, Th. Udem, *Phys. Rev. A* **81**, 033427 (2010).
24. A. Ozawa, Y. Kobayashi, *Phys. Rev. A* **86**, 022514 (2012).
25. H. Wang, A. M. Weiner, *IEEE J. Quantum Electron.* **39**, 1600–1618 (2003).
26. G. Hagel, R. Battesti, F. Nez, L. Julien, F. Biraben, *Phys. Rev. Lett.* **89**, 203001 (2002).
27. D. C. Yost *et al.*, *Phys. Rev. A* **90**, 012512 (2014).
28. H. Fleurbaey, F. Biraben, L. Julien, J. P. Karr, F. Nez, *Phys. Rev. A* **95**, 052503 (2017).
29. U. D. Jentschura, V. A. Yerokhin, *Phys. Rev. A* **73**, 062503 (2006).
30. The NIST Reference on Constants, Units, and Uncertainty, CODATA Internationally recommended 2018 values of the Fundamental Physical Constants; https://physics.nist.gov/cuu/Constants/index.html.
31. V. A. Yerokhin, K. Pachucki, V. Patkóš, *Ann. Phys.* **531**, 1800324 (2019).
32. A. Antognini *et al.*, *Science* **339**, 417–420 (2013).
33. R. W. P. Drever *et al.*, *Appl. Phys. B* **31**, 97–105 (1983).
34. A. Grinin, Data for the 1S-3S measurement, Version 1, Zenodo (2020); https://doi.org/10.5281/zenodo.4046497.

ACKNOWLEDGMENTS

We thank J. Weitenberg, S. Karshenboim, K. Pachucki, and V. Yerokhin for helpful discussions. **Funding:** Support was provided by the Deutsche Forschungsgemeinschaft (German Research Foundation DFG) under Germany's Excellence Strategy, project EXC-2111-390814868, and the DFG Cluster of Excellence PRISMA+ (EXC 2118/1 project 39083149). **Author contributions:** T.U. planned the experiment, and T.U., R.P., and T.W.H. supervised the experiment. A.G. and A.M. obtained the data. A.G., A.M., D.C.Y., L.M., and V.W. worked on setting up the experiment. A.M., A.G., and T.U. did the modeling. A.G., A.M., and T.U. carried out the data analysis. All authors contributed to the analysis of the systematic uncertainties and to writing the manuscript. **Competing interests:** None declared. **Data and materials availability:** All data needed to evaluate the conclusions in the paper are present in the paper or the supplementary materials. The raw data and description of the data are available at Zenodo (*34*).

SUPPLEMENTARY MATERIALS

science.sciencemag.org/content/370/6520/1061/suppl/DC1
Supplementary Text
Figs. S1 to S34
Tables S1 to S3
References (*35*–*63*)

14 May 2020; accepted 14 October 2020
10.1126/science.abc7776

Two-photon frequency comb spectroscopy of atomic hydrogen

Alexey Grinin, Arthur Matveev, Dylan C. Yost, Lothar Maisenbacher, Vitaly Wirthl, Randolf Pohl, Theodor W. Hänsch and Thomas Udem

Science **370** (6520), 1061-1066.
DOI: 10.1126/science.abc7776

Testing physics using the hydrogen atom

Discrepancy between the proton radius determined from hydrogen and muonic hydrogen spectroscopy data, the so-called "proton radius puzzle," has been a focus of the physics community for more than a decade now. Using two-photon ultraviolet frequency comb spectroscopy below 1 kilohertz, Grinin *et al.* report a high-precision measurement of the 1S-3S transition frequency in atomic hydrogen (see the Perspective by Ubachs). Combining this measurement with the data for the 1S-2S transition, the authors obtained the Rydberg constant with improved accuracy and an independent value for the proton charge radius that favors the data from muonic hydrogen. However, the present frequency value differs from the one obtained previously using a different spectroscopic technique, leaving the puzzle still unresolved.

Science, this issue p. 1061; see also p. 1033